Article

Not peer-reviewed version

NanoBioAnalytical (NBA) platform to decipher extracellular vesicles secreted by microvascular endothelial cells under benzo[a]pyrene exposure

Geetika Raizada , Joan Guillouzouic , Alain Rouleau , Eric Lesniewska , Eric Le Ferrec , Céline Elie-Caille , Wilfrid Boireau *

Posted Date: 9 January 2025

doi: 10.20944/preprints202501.0599.v1

Keywords: Extracellular vesicles (EVs); cytotoxicity; polycyclic aromatic hydrocarbons (PAH); surface plasmon resonance imaging (SPRi); atomic force microscopy (AFM)

Article

NanoBioAnalytical (NBA) Platform to Decipher Extracellular Vesicles Secreted by Microvascular Endothelial Cells Under Benzo[a]pyrene Exposure

Geetika Raizada [1], Joan Guillouzouic [2], Alain Rouleau [1], Eric Lesniewska [3], Eric Le Ferrec [2], Céline Elie-Caille [1] and Wilfrid Boireau [1,*]

[1] FEMTO-ST Institute, CNRS, ENSMM, UTBM, 15B Avenue des Montboucons, 25030 Besançon, France

[2] Univ Rennes, Inserm, EHESP, Irset (Institut de Recherche en Santé Environnement et Travail), UMR_S 1085, F-35000, Rennes, France

[3] ICB UMR 6303 CNRS, University of Bourgogne Franche-Comté, F-21078 Dijon, France

* Correspondence: wilfrid.boireau@femto-st.fr

Abstract: Recent advancements in the clinical EV field highlight their potential as biomarkers for diverse diseases and therapeutic applications. This study provides an in-depth characterization of 10K EVs from human microvascular endothelial cells (HMEC-1) exposed to benzo-a-pyrene (B[a]P), a polycyclic aromatic hydrocarbon found in food and smoke. Given EVs' complexity, with numerous surface and cargo proteins, phenotyping remains challenging. Here, we introduce a multiplex biosensor for profiling EVs from distinct cellular conditions, employing a multimodal approach that integrates surface plasmon resonance imaging (SPRi) and atomic force microscopy (AFM) to examine how cytotoxic environments impact EV biochemical and biophysical properties. SPRi experiments showed notable Evs capture differences ion ligands as Anti-CD36, Anti-CD81, and Anti-ApoA between treated and control conditions, likely due to B[a]P exposure. Complementary AFM scanning and statistical analyses revealed size differences between EVs from treated and control samples, with ligands like Anti-CD81, Anti-ApoA, Annexin-V, Anti-NOX2, and Anti-VEGFR1 emerging as ligands specific to potential cytotoxicity biomarkers. Our findings suggest that B[a]P exposure may increase EV size and alter marker expression, indicating phenotypic shifts in EVs under cytotoxic stress. This study highlights the utility of SPRi and AFM in identifying EV markers linked to cytotoxic responses, providing insights into EV heterogeneity in stress conditions.

Keywords: extracellular vesicles (EVs); cytotoxicity; polycyclic aromatic hydrocarbons (PAH); surface plasmon resonance imaging (SPRi); atomic force microscopy (AFM)

1. Introduction

Extracellular vesicles (EVs) are proteo-lipidic membranous particles released into extracellular environments from almost all types of cells, they are known to play an important role in intercellular communication and transfer the material from the originating cells to the host cells [1,2]. Because of their presence in various biological fluids including but not limited to blood, urine, saliva and cerebrospinal fluid, they are currently explored for their potential application as biomarkers in various pathologies. They are known to contain nucleic acids, lipids, proteins, and in some cases organelles in their cargo [3,4]. This versatility has sparked significant interest in their use as biomarkers for toxicant exposure, as EVs can reflect cellular responses to environmental contaminants and provide insights into the mechanisms of toxicity. This potential has driven research into the role of EVs in responding to environmental pollutants, particularly those with widespread exposure and significant health impacts [5]. Among these, benzo[a]pyrene (B[a]P), a polycyclic aromatic hydrocarbon (PAH), has emerged as a key focus due to its well-documented cytotoxic,

 doi:10.20944/preprints202501.0599.v1

mutagenic, and carcinogenic properties [6]. Exposure to B[a]P induces cytotoxicity through the formation of protein and DNA adducts, as well as oxidative stress resulting from the overproduction of reactive oxygen species (ROS) [7]. The toxic cellular environment induced by B[a]P triggers complex responses that extend beyond the directly affected cells, impacting neighboring cells through alterations in the cellular microenvironment [5]. EVs released from affected cells may carry oxidized lipids, altered proteins, and damaged or modified DNA, potentially exerting harmful effects on recipient cells [8]. EVs may also serve a protective role for the originating cells; however, they can simultaneously propagate damage to neighboring cells through a bystander effect by transferring modified proteins, DNA adducts, or bioactive metabolites [9]. EVs are central to the cellular response to oxidative stress, playing a critical role in balancing cellular homeostasis and propagating damage within the microenvironment. This dynamic response gives rise to diverse biogenesis mechanisms, altered protein expression, and ultimately, the formation of distinct EV subpopulations.

Several technologies like Western Blot, ELISA, and Flow Cytometry are commonly used for EV detection and characterization [10]. While these techniques are reliable, they often come with challenges such as being time-consuming, requiring large sample volumes, and involving intricate labeling procedures. In order to overcome these limitations and to address the discrimination of small changes in the different EV sub populations There is a growing shift towards label-free detection methods in a multiplex format. Techniques such as optical sensors, including plasmonic and interferometric sensing, as well as electrochemical sensors like potentiometry, potentiostatic, glavanostatic and impedance spectroscopy, are gaining prominence for their ability to enable efficient and rapid analysis of EVs. The main principle behind these methods is based on biomolecular interactions between biologic or synthetic receptors—such as antibodies, aptamers or chemical ligands—and EV surfaceome for the specific capture of EV subpopulations [11].

Surface Plasmon Resonance (SPR), a well-established optical label-free biosensing technology, enables the study of biomolecular interactions between immobilized biomolecules and biological targets with high sensitivity at the vicinity of the gold surface (<250 nm), making it an ideal tool for EVs characterization[12]. The multiplexing provided by this technique also allows simultaneous EV subpopulation detection and quantification by using a panel of surface-immobilized antibodies [13]. Several studies have demonstrated the usefulness and relevancy of SPRi biosensors for detecting various diseases, including cancer and Alzheimer's disease, through EV analysis [14,15], [16]. Due to the complex composition and heterogeneous nature of EVs, it is of interest to combine SPR with other technologies to improve their qualification. *Hsu et al*. integrated SPR with surface plasmon-enhanced fluorescence spectroscopy (SPEFS) to simultaneously detect protein and miRNA content in tumor-derived EVs [17]. In our group, previously Obeid et al. have developed nano-bio-analytical (NBA) platform which combined SPRi with AFM and mass spectrometry where they analyzed thrombin activated platelet EVs related to transfusion safety [18]. However, a significant challenge in detecting EV subpopulation lies in the expression of hundreds of proteins on their surfaces, adding complexity to their characterization.

In this study, we selected different proteins known to be present on the surface of EVs produced by endothelial cells, with the aim of determining whether our approach allows us to detect them and whether the EVs produced by endothelial cells in the presence of B(a)P exhibit a modified 'surfaceome'. Building on the NBA platform previously developed in our group [18,19], we employed a multimodal approach combining SPRi and AFM. SPRi facilitated the identification of EV phenotypes by using specific ligands (antibodies and proteins) grafted onto a biochip, enabling immunocapture while maintaining EV structural integrity. To address the complexity posed by the vast array of surface proteins, we expanded the range of ligands for selective EV capture by miniaturizing the ligand spots on the biochip. This was accomplished through the implementation of automatic nano-spotting greatly enhancing the multiplexing capacity. Complementing this, AFM provided precise metrological data on the selectively captured EVs, linking surface protein expression to their morphological and structural features, thereby enabling a highly discriminative characterization of EV subpopulations.

 doi:10.20944/preprints202501.0599.v1

2. Materials and Methods

2.1. Cell Culture and EV Isolation

The method of cell culture and EV isolation was described by *Le Goff et al*. [20]. Human microvascular endothelial cell line (HMEC-1) was sourced from the Center for Disease Control and Prevention, Altanta, USA; the cells were cultured in endothelial basal medium MCDB131 (US Biological Life Sciences, Ref E3000-01G) which incorporated 10% heat deactivated (56°C, 30min) fetal bovine serum (FBS, Dutscher, Ref 500105A1A), L-glutamine (Gibco, Ref 25030, 10mM final), penicillin/streptomycin (Gibco, Ref 15140-122, 100 unit/mL final), gentamycin (Gibco, Ref 15750-037, 500µg/mL final), epithelial growth factor (EGF, Sigma, Ref E9644, 10ng/mL final) and Hydrocortisone (Up John, Ref 3400932141159, 1µg/mL final) in 151.9 cm2 petri dishes (Corning, Ref 353025). The medium's pH was adjusted to 7.6 using sodium bicarbonate (Gibco, Ref 25080-060) and replaced every 2–3 days. Cells were passaged weekly through trypsinization (trypsin EDTA 0.05%, Gibco, Ref 25300-054). Upon reaching 90% confluence, the cells were incubated overnight in FBS-free medium. The following day, they were treated with 100 nM Benzo[a]pyrene (B[a]P, Sigma, Ref B1760) dissolved in DMSO (Sigma, Ref D8418), ensuring the final DMSO concentration did not exceed 0.0005% (v/v) (treated condition). Control cultures received the same volume of DMSO without B[a]P (control condition).

For 10K EVs isolation, international guidelines for EV isolation was followed [21]. Conditioned media was centrifuged at 3650 × g for 10 minutes at 4°C to remove cells and debris. The clarified supernatant was transferred into ultracentrifugation tubes (Beckman Coulter, 5/8 × 4 P.A tube, 17 mL, Ref.: 337986). To adjust the volume as needed, sterile 1X PBS verified as EV-free by Nanoparticle Tracking Analysis (Gibco, DPBS 1X, Ref.: 14190-094) was added. EVs were pelleted by ultracentrifugation at 10,000 × g for 30 minutes at 4°C using an Optima L-90 K ultracentrifuge with Sw 28.1 Ti rotor or XE-90 ultracentrifuge with Sw 32 Ti rotor (Beckman Coulter, USA).

After removing the supernatants, the 10K EV pellets were washed by resuspension and, if required, pooled into a single ultracentrifugation tube per treatment condition. Following volume adjustment with 1X PBS, a second ultracentrifugation step was performed at 10,000 × g for 30 minutes at 4°C. The final 10K EV pellet was resuspended in 50 µL of 1X PBS and stored at -20°C. EV concentration was determined using Nanoparticle Tracking Analysis (NanoSight NS300, Malvern Instruments, UK) following a protocol of five 60-second video recordings.

2.2. SPRi Biochip Preparation

SPRi biochips were fabricated by FEMTO Engineering in the MIMENTO clean room facility following the previously described method [19,22]. These biochips were composed of glass slides (SF11) with a thin coating of gold (48 nm) and titanium (2 nm) as an adhesive layer in between. The biochips were then chemically functionalized by incubating overnight the mixture of mercapto-1-undecanol (11-MUOH: C11) and mercapto 1-hexadecanoic acid (16-MHA: C16) with the ratio of 80:20 by mole. It was followed by the activation of the biochip using EDC-NHS chemistry by incubating the biochip in the mixture of 200 mM ethyl (dimethylaminopropyl) carbodiimide/ N hydroxysuccinimide (EDC) and 50 mmol/L N-hydroxysuccinimide (Sulfo-NHS) for 30 min in the dark at room temperature. This step facilitated the activation of NHS esters, enabling the covalent grafting of proteins or antibodies by forming a bond between the amine (-NH2) groups and the NHS esters.

2.3. Automated Ligand Spotting and Biochip Pattern

After activating the biochip, the next step was to graft chosen ligands (Table 1). We employed the nano spotter system (sciFLEXARRAYER by *Scienion*) to deposit small volumes of ligands at the designated place. This system operates on the principle of non-contact liquid dispensing via a piezo dispense capillary (PDC). For the experiments, PDC70 was utilized with the following parameters:

 doi:10.20944/preprints202501.0599.v1

91 V, 47 µs pulse duration, 500 Hz frequency, and 200 µs LED delay. A volume of 3 nl was deposited for each spot.

Table 1. List of chosen ligands with their grafting pH.

Antibodies/Protein grafted	Manufacturer (Ref)	Grafting pH
Annexin-V	Biovision (1005-100)	7
Anti-CD63	Diaclone (857.770.000)	5.5
Anti-CD9	Abcam (Ab2215)	6
Anti-CD81	Invitrogen (MA1-10290)	4
Anti-CD44	Biolegend (103001)	4.5
Anti-CD36	Invitrogen (MA5-30176)	4.5
Anti-NOX2	Abcam (EPR24537-56)	4.5
Anti-Enolase 1	Santa Cruz (SCBT SC- 151013)	7
Anti-ApoA	Invitrogen (MIA1405)	4
Anti-VEGFR1	Abcam (ERP21886-207)	6
Anti-OVA (negative control)	Sigma-Aldrich (A6075)	4.5

The following pattern (Figure 1) of 100 spots (10 rows × 10 columns) was printed, with each spot measuring approximately 200 µm in diameter and spaced 600 µm apart. Anti-OVA was alternated as a negative control, while ligands of interest were arranged in vertical rows to minimize spotting time and account for mass transfer effects, ensuring consistent sample availability across the biochip.

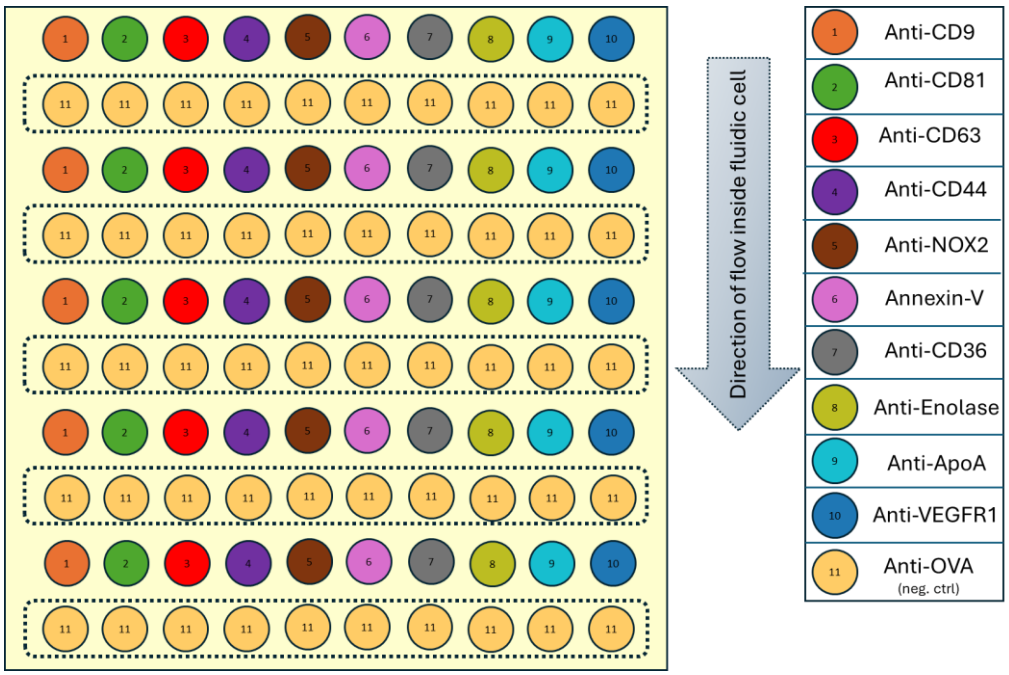

Figure 1. Biochip design with 100 miniaturized spots of 11 different ligands.

2.4. Immunocapture Experiments: SPRi

The subsequent steps following ligand grafting are thoroughly detailed in our previous work [19] and are all monitored inside the SPR apparatus ensuring very high quality controls. The immunocapture SPRi experiment can be divided into two main phases: passivation and deactivation of biochip and kinetic monitoring of sample interactions.

All the experiments were done on Horiba SPRi Plex II system, using running buffer HEPES 10mM (Sigma-Aldrich, H3375-100G) + $CaCl_2$ 5 mM (Sigma-Aldrich, 223506-500G) buffer solution.

 doi:10.20944/preprints202501.0599.v1

Sample containing EVs (concentration ~ 10^8 particles/ml) were injected at 10 µl/min for 20 min. After observing the sample interaction with different ligands and having a stable baseline, glutaraldehyde (0.5%) was injected at 20 µl/min for 10 mins to fix the EVs captured on the biochip. This fixed biochip was then further characterized with AFM for obtaining size profile and density of EVs captured.

2.5. AFM Characterization

AFM imaging was conducted using the Bruker Nanowizard®4 Bioscience system in tapping mode (AC mode) in air, employing triangular Pyrex-Nitride AFM tips (spring constant: 0.08 N/m). After aligning the laser on the AFM tip and optimizing the SUM value, we calibrated the tip in air before engaging the sample surface. Using the AC Feedback mode wizard, we performed a frequency sweep (Lock-in Phase vs. Frequency) to determine the optimal drive frequency and set point. By specifying the drive amplitude (typically around 20 nm) and the frequency range, we identified the best settings for stable oscillation and precise feedback control, usually setting the set point to 70–80% of the drive amplitude. This ensured reliable operation for high-quality imaging or measurements. During the scanning, further adjustments were made as necessary. Images were captured at a line rate of 1 Hz with a resolution of 512 × 512 pixels. Initial scans covered a 10 × 10 µm area to examine the surface, followed by detailed 2 × 2 µm scans used for particle counting and size profiling.

Image analysis was carried out using Mountain's SPIP 9 software, utilizing the "Particle Analysis" function to measure object counts and profile their size based on maximum diameter and height. To ensure that only EVs adhered to the surface were analyzed, a dynamic height threshold of 8.5 nm was applied, excluding objects smaller in height than 8.5 nm and an additional projected area threshold was implemented to disregard objects with areas smaller than 200 nm^2. These filtering steps effectively isolated EVs in the AFM images, ensuring precise size and count measurements [23].

2.6. Statistical Analysis

A python code was written to extract the data and obtain different curves like plasmon curves, kinetic data and response obtained at different families of ligands. Afterwards the plasmon curves were analysed to quantify ligand grafting by measuring the angular shift between the ligand and the biochip surface. An alternative method involved assessing the reactivity of RSA during the passivation step, where ambiguous results were excluded by verifying that a significant amount of RSA was not grafted onto the ligand, indicating proper ligand grafting. To minimize the impact of non-specific interactions, the SPRi response for each ligand was adjusted by subtracting the average response from negative control ROIs.

To ensure consistency across experiments, SPRi responses for different ligands were normalized to account for sample variability and preparation inconsistencies. The reference for normalization was selected based on its low variability, determined as the ratio of the standard deviation to the mean response across experiments. Anti-CD44, which exhibited the most stable and reproducible response with ratios of 0.48 and 0.43 for control and treated conditions, respectively, was chosen as the normalization reference. This was based on its low variability, calculated as the ratio of the standard deviation to the mean response across experiments. Responses for other ligands were normalized by dividing their values by the response of Anti-CD44, which consistently maintained a fixed value in the phenotype profile. This normalization approach provided a reliable baseline for comparing ligand interactions, reducing variability, and enhancing the accuracy of the data.

To explore differences between the two conditions using AFM data, we conducted an independent t-test to assess whether the means of the two groups were statistically different. This test evaluates the null hypothesis (H_0), which assumes no significant difference between the groups, against the alternative hypothesis (H_1), which posits a significant difference. A p-value less than 0.05 indicates rejection of the null hypothesis, confirming a significant difference. The t-test was performed for each ligand to compare AFM data between the control and treated conditions, identifying whether significant differences in EV capture were present for specific ligands. The

 doi:10.20944/preprints202501.0599.v1

analysis was implemented using the "*scipy.stats*" module and the "*ttest_ind*" function in Python, ensuring robust statistical evaluation of the data.

3. Results

3.1. Kinetic Monitoring of Sample Interactions

The immunocapture experiments were conducted on the sample originating from both control and treated conditions. The study aimed to evaluate the differences in ligand interactions with samples from two conditions, enabling a comparative analysis under consistent experimental parameters. Anti-CD81, Anti-CD63, and Anti-CD9 were selected as markers for EVs. Annexin V was chosen for its ability to bind phosphatidylserine, which is present on microvesicles. Anti-CD44, Anti-CD36, and Anti-VEGFR1 were used as markers for endothelial cells. Anti-NOX2 and Anti-Enolase, while expressed in endothelial cells, were included due to their involvement in toxic mechanisms associated with exposure to environmental contaminants. Anti-ApoA was included in our chip pattern as a control, similar to how we use Anti-OVA as a negative control.

Figure 2a,c illustrate the kinetic curves from two experiments conducted on samples from the control and treated conditions, respectively, depicting the variation in reflectivity (%) over time (minutes) during sample injection (10^8 particles/ml). An initial increase in reflectivity is observed, followed by distinct interaction patterns as the injection continues, with each ligand family exhibiting unique interactions with the EVs. (Note: Anti-Enolase was excluded from the analysis due to its lack of response which raised uncertainty about its specificity and rendered it unsuitable for the study). The response (Figures 2b and 2d) was calculated using the formula "End signal – Start signal," where the end signal represents the stabilized reflectivity variation after the injection, and the start signal denotes the reflectivity variation before the injection began. These points are marked by the dotted blue and red lines in Figures 2a and 2c, respectively.

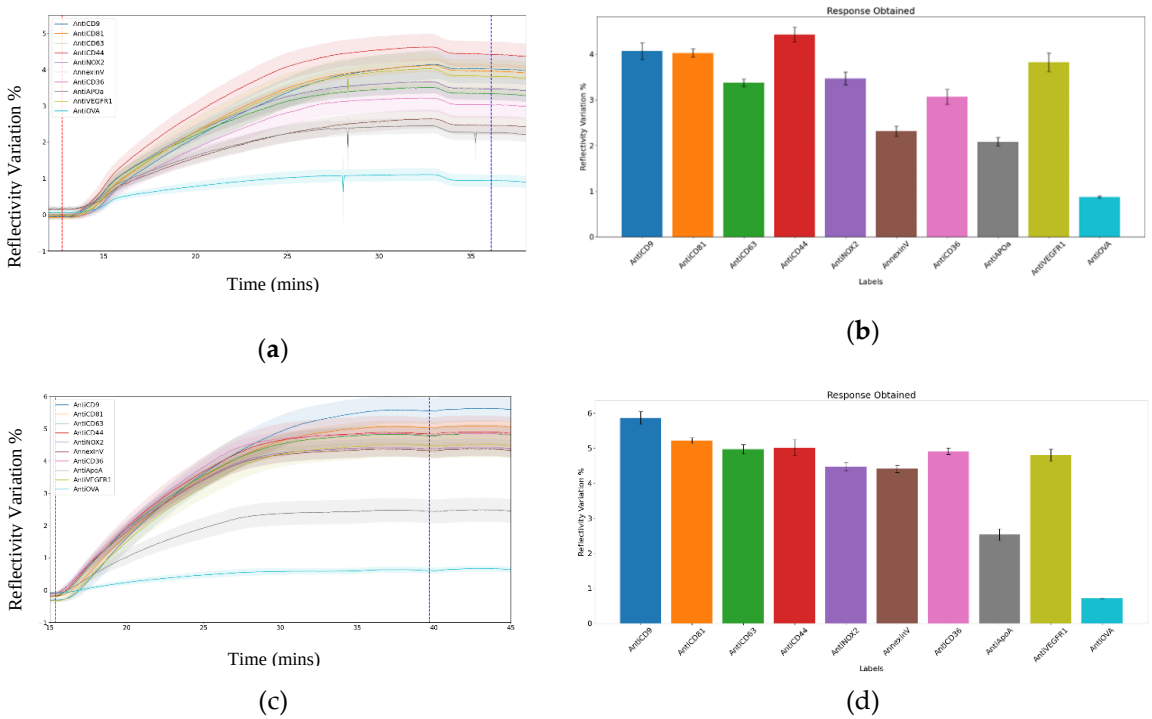

Figure 2. Sensorgrams and responses measured on different ligands following 10K EV sample injection (10^8 EVs/ml at 10 µl/ml). (a) Sensorgram from one of the experiments conducted under the control condition and (b) the corresponding response. (c) Sensorgram from a sample injection (from one experiment) under the treated condition and (d) the calculated response. The shaded areas in the sensorgrams represent the standard deviation across different spots for a given ligand. The red and blue dotted lines indicate the start and end points used to calculate the response for each ligand.

 doi:10.20944/preprints202501.0599.v1

Each ligand family was analysed using five spots, while the negative control included a total of 50 spots, providing robust statistical data for comparison. The low standard deviation observed for the negative control confirmed the reliability of the experimental setup and the measured responses.

Multiple experiments were conducted for each condition, and those with consistent parameters, such as identical sample concentrations, were selected for analysis. This resulted in the inclusion of five experiments for the control condition and four for the treated condition. The responses from the ligands were highly specific, showing a difference of over 200% compared to the negative control, demonstrating effective ligand-based capture.

On-Chip Phenotype Profiling

To generate the phenotype profile, responses were calculated as previously described (see sub-part 2.6), followed by normalization using a statistical approach to ensure comparability across experiments. The resulting profile was derived from the normalized average SPRi response for each ligand, as illustrated in Figure 3.

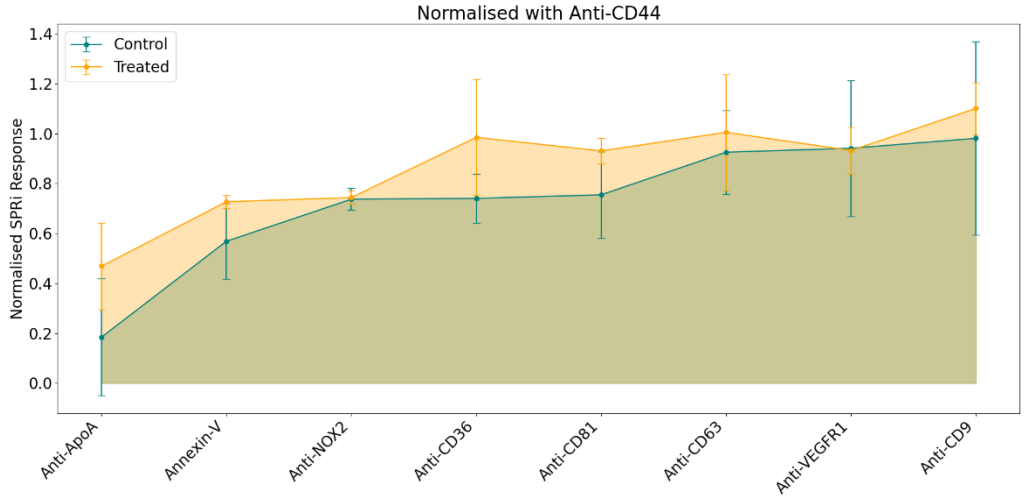

Figure 3. Normalized SPRi responses obtained on multiplexed biochip for large EVs samples originating from control (blue) and treated (orange) conditions.

The general pattern in the phenotype profile indicated a stronger SPRi response in samples from the treated condition despite injecting similar concentration of EVs (10^8 particles/ml) for both samples. Among the panel of selected ligands, the most notable variations were observed with Anti-CD36, Anti-CD81, and Anti-ApoA. In comparison, Annexin V, Anti-CD63, and Anti-CD9 exhibited only minor differences. Conversely, no differences were detected in the responses for Anti-NOX2 and Anti-VEGFR1.

3.2. AFM Data: Metrology

Following SPRi analysis, according to the hyphenated procedure originated in the team, the conditioned biochips were characterized with the help of AFM. This technique offers high-resolution imaging, enabling detailed visualization of variations in EV morphology across different conditions. The resulting images can reveal differences in particle number, size, shape, or surface characteristics, which may correlate with the SPRi response variations or provide novel insights. These insights could include changes in EV topology or dimensions, such as height or maximum diameter, potentially which could be attributed to the presence of B(a)P in the culture medium during their production by the cells.

 doi:10.20944/preprints202501.0599.v1

The following AFM topographical (height) images (Figure 4) were obtained at different ligands spotted on biochip, revealing that EVs generally exhibit a round or elliptical shape. Elliptical morphology may result from interactions between the antibodies and the EVs, potentially leading to their elongation. Notably, a small number of large EVs were observed alongside the predominance of small EVs across all ligands. During the scanning of negative control spots, some objects were detected, likely arising from non-specific interactions. However, their density was significantly lower compared to the ligand-specific images. AFM images of the ligand spots were captured at a size of 2x2 μm^2, while those of the negative control were taken at 10x10 μm^2. This disparity in object density aligns with and further supports the SPRi response observed.

 doi:10.20944/preprints202501.0599.v1

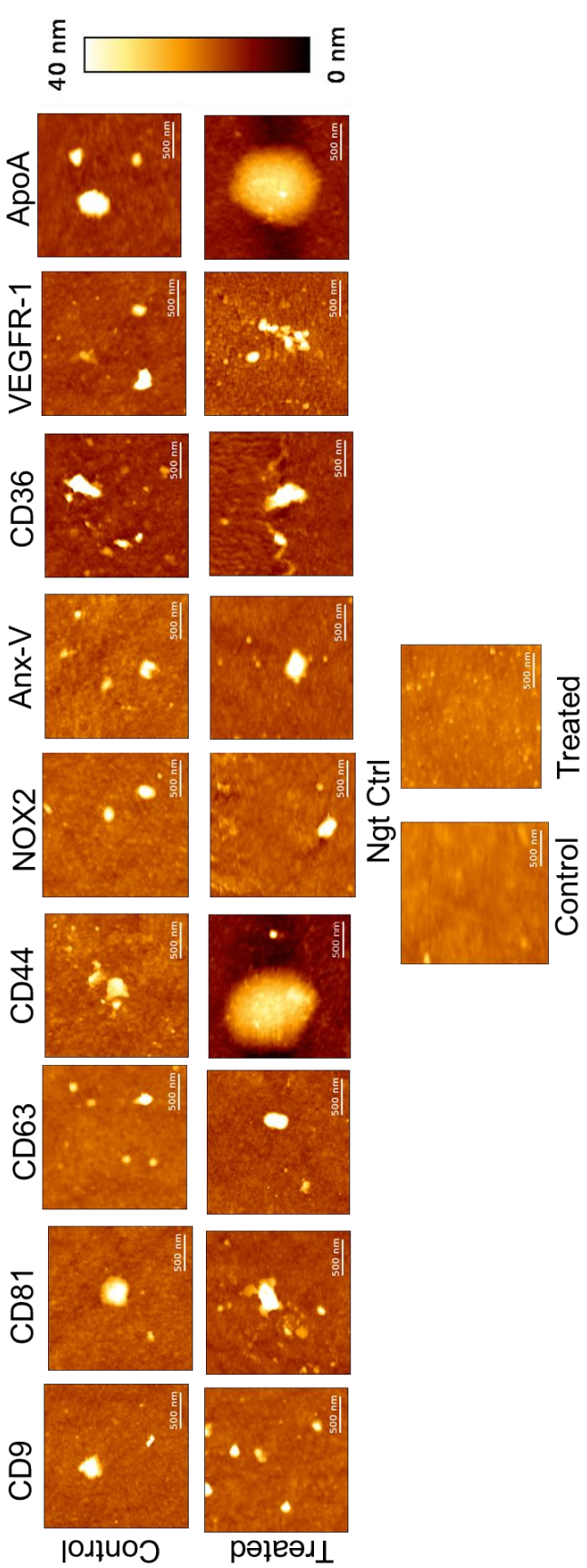

Figure 4. AFM topological images obtained on the EVs captured at different ligands originating from control and treated conditions (with the z-scale 40 nm for all the images).

 doi:10.20944/preprints202501.0599.v1

The size profile was obtained using the "*Particle Analysis*" module in *Mountain's SPIP 9* software. Parameters such as maximum diameter and height were analysed to examine differences between EVs derived from the two conditions. In Figure 5, the split violin plot provides a visual representation of these differences, where the left half (blue) illustrates the height distribution of control EVs, and the right half (orange) depicts the maximum diameter and height distribution of treated EVs. The width of each violin reflects the density of EV measurements, with wider sections indicating a higher concentration of EVs within a particular size range.

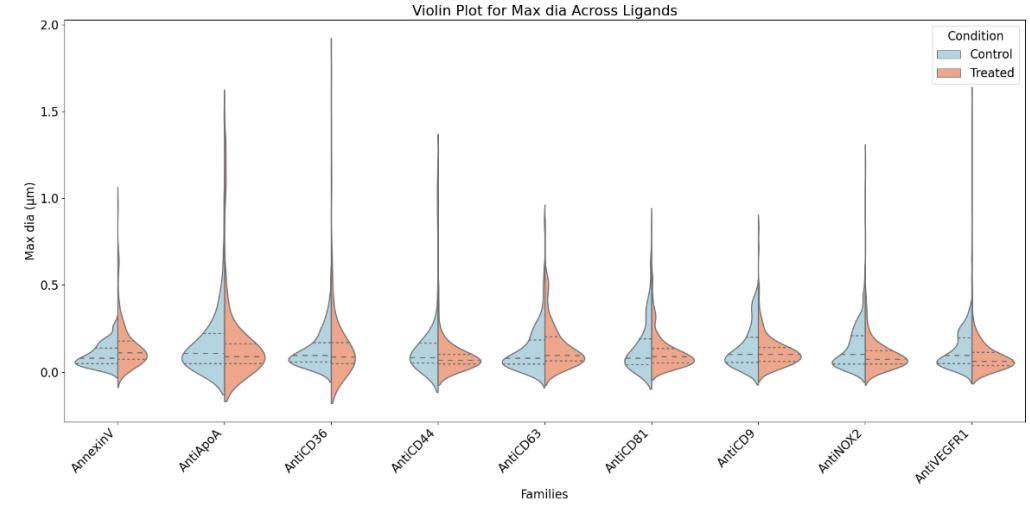

(**a**)

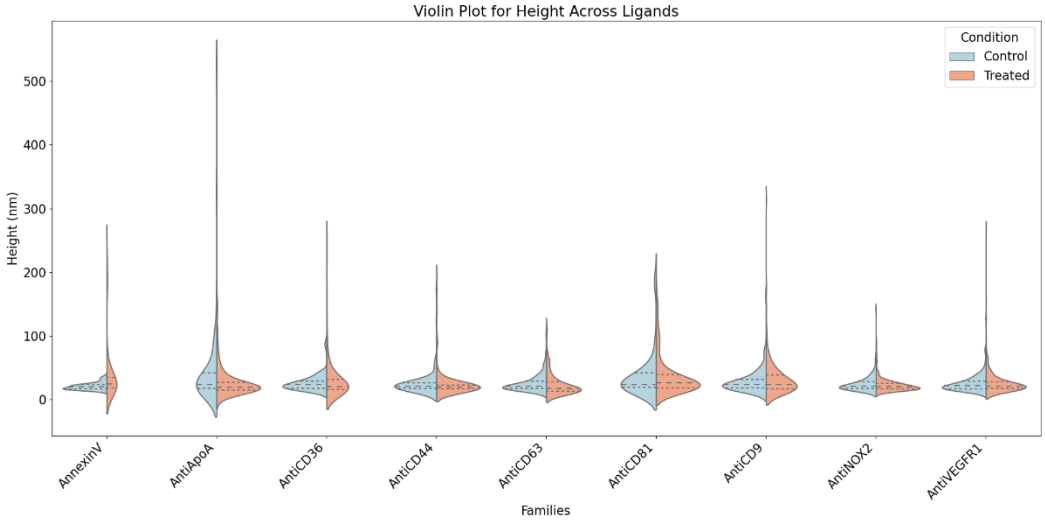

(**b**)

Figure 5. Split violin plot of size distribution: (**a**) maximum diameter (µm); (**b**) height (nm), where middle dashed line is median, and the outer dashed lines are 25th and 75th percentiles. Blue: control & orange: treated.

The analysis identified Anti-ApoA, Anti-CD36, and Annexin-V as the most affected ligands. Treated EVs associated with Anti-ApoA exhibited larger diameters and greater variability, along with subtle increases in height, suggesting a moderate response to treatment, primarily in diameter. Anti-CD36-associated EVs showed significant increases in both diameter and variability, with slight height variability, indicating sensitivity to treatment effects, especially in diameter. Annexin-V-associated EVs displayed broader distributions and higher diameters in the treated condition, accompanied by slight increases in height variability, demonstrating consistent treatment effects on both diameter and height.

Moderately affected ligands included Anti-CD44 and Anti-NOX2. Anti-CD44-associated EVs exhibited significantly larger diameters and broader distributions in the treated condition, with no notable changes in height, indicating that treatment predominantly affects diameter. Anti-NOX2-

 doi:10.20944/preprints202501.0599.v1

associated EVs showed minimal differences in diameter but a slight upward shift in height for treated EVs, indicating mild treatment effects, mainly on height. Unaffected ligands, including Anti-CD63, Anti-CD9, Anti-CD81, and Anti-VEGFR1, showed similar diameter and height distributions between control and treated conditions, suggesting these ligands represent stable EV subpopulations unaffected by treatment.

Following the global analysis of EVs captured on various ligands, a t-test analysis was applied specifically to large EVs with a maximum diameter greater than 0.2 μm to evaluate whether the same or different patterns were observed within this selective EV subpopulation. This analysis aimed to identify statistically significant differences in size between the two conditions, control and treated. The results revealed notable differences for specific markers. Anti-NOX2 exhibited a significant increase in "Maximum Diameter" in the treated condition, with a marginally non-significant trend observed for "Height." Anti-VEGFR1 showed significant differences in both "Maximum Diameter" and "Height," with the treated condition presenting larger values, particularly in height. Additionally, markers such as Anti-CD81 and Anti-CD36 displayed significant differences in either "Maximum Diameter" or "Height," further highlighting treatment-induced effects. However, some markers, including Anti-CD9 and Anti-CD63, did not exhibit any significant differences between the two conditions. This analysis underscores the targeted impact of treatment response across different EV subpopulations and ligands.

Table 2. Table summarizes the t-test results on large EVs.

Ligands	Title 2	T-statistic	p-value	Significant differences
Anti-CD9	Maximum diameter	-0.417	0.678	++
	Height	-2.047	0.046	
Anti-CD81	Maximum diameter	2.099	0.040	+
	Height	-0.233	0.817	
Anti-CD63	Maximum diameter	-1.098	0.276	=
	Height	-1.724	0.089	
Anti-CD44	Maximum diameter	0.005	0.996	=
	Height	-1.562	0.132	
Anti-NOX2	Maximum diameter	-2.621	0.011	++
	Height	-1.970	0.052	
Anti-CD36	Maximum diameter	-2.560	0.014	++
	Height	-2.848	0.007	
Annexin-V	Maximum diameter	-1.440	0.159	++
	Height	-2.246	0.031	
Anti-VEGFR1	Maximum diameter	-2.311	0.024	++
	Height	-3.822	0.000	
Anti-ApoA	Maximum diameter	-1.906	0.061	++
	Height	0.885	0.379	

* ++: Highly significant; +: significant; =: no difference.

The heat maps (Figure 6) reveal a broader distribution of EV sizes in the treated condition, indicating a shift toward large EVs. This trend is prominent in ligands such as Anti-NOX2 and Anti-CD36, suggesting that treatment promotes the generation of larger EVs. In contrast, the control condition showed a more confined large EV distribution, with Annexin V displaying a higher concentration of large EVs around 200–300 nm. These findings highlight treatment-specific effects on EV size and abundance across specific ligands, complementing the t-test results.

 doi:10.20944/preprints202501.0599.v1

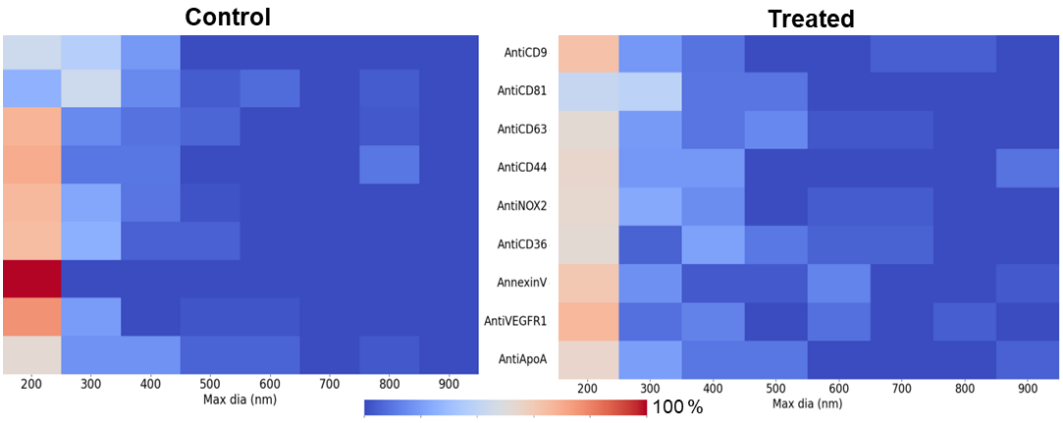

Figure 6. Heat maps based on AFM results to display the maximum diameters of large EVs captured on various ligands. The bin size for these heatmaps is set at 100 nm, with each bin representing the EVs falling within the size range specified on the x-axis.

4. Discussion

Through this study, we obtained insights into EVs subpopulations' biophysical properties under different conditions, revealing distinct patterns linked to specific surface protein expression. By employing NBA platform which comprises advanced analytical techniques such as AFM and SPRi, coupled with statistical evaluations, we have characterized EV subpopulations, focusing on ligand-specific interactions and size-related parameters. This comprehensive approach has allowed us to uncover treatment-induced changes in EV ligand binding and EVs morphology, shedding light on the underlying biological mechanisms and the potential diagnostic value of EVs in distinguishing between conditions.

Beyond the general trend of a higher SPRi response for treated EV samples, significant differences in EVs capture were observed for the ligands Anti-CD36, Anti-CD81, and Anti-ApoA, which could be correlated to cellular response to B[a]P exposure. CD36 plays a vital role in scavenging damaged or dying cells, regulating inflammation, and modulating pro-apoptotic and anti-angiogenic signalling pathways. It is crucial in managing cellular stress responses by recognizing apoptotic markers, such as phosphatidylserine (PS), on the surface of damaged cells [24,25]. The elevated response observed with Anti-CD36 suggests the presence of CD36+ EVs, potentially reflecting cellular mechanisms to clear apoptotic debris and regulate inflammatory responses triggered by cytotoxic stress induced by pollutant exposure. AFM observations further support this, showing a broader distribution of large EVs in the treated condition, particularly for Anti-CD36, indicating treatment-induced changes in EV morphology.

Similarly, the elevated response on Anti-ApoA in the treated condition may indicate increased expression of ApoA-I, likely representing a protective mechanism against oxidative and inflammatory damage caused by B[a]P [26]. As a key component of high-density lipoprotein (HDL), ApoA-I plays an essential role in reverse cholesterol transport, removing excess cholesterol and lipids from cells, particularly under stress conditions [27]. ApoA-I also helps reduce ER stress and apoptosis [28], mitigating some of the cytotoxic effects triggered by B[a]P exposure. The increased response observed for Anti-CD81, Anti-CD63, and Anti-CD9 in the treated condition compared to controls may be attributed to the elevated production of vesicles under cytotoxic stress. Alternatively, it is also possible that these markers are more densely expressed on EVs from the treated condition, leading to higher interaction values.

Interestingly, the broader size distribution observed in the heat maps for ligands like Anti-NOX2 and Anti-CD36 further corroborates the generation of larger EVs in the treated condition, reflecting treatment-induced effects on EV morphology and abundance. NADPH oxidase 2 (NOX2) plays an important role in regulating reactive oxygen species [29] and due to the B[a]P exposure, it might play

 doi:10.20944/preprints202501.0599.v1

an pivotal role in cytotoxicity. However, some markers, such as Anti-CD9 and Anti-CD63, displayed consistent distributions across all conditions, highlighting the relevancy of this markers for EVs characterization through the NBA platform.

Although the overall size and abundance trends align with treatment-induced cytotoxic stress, specific markers like Anti-VEGFR1 and Anti-NOX2 provide additional insights into differential EV responses. Anti-VEGFR1 showed significant differences in both maximum diameter and height, particularly under the treated condition, suggesting changes in EV biophysical properties or higher production of certain EV subpopulation. In contrast, Anti-NOX2 demonstrated a significant increase in maximum diameter while maintaining a consistent SPRi response, underscoring the importance of combining multiple techniques to fully understand EV behavior. The unchanged cumulative SPRi response on Anti-NOX2 between control and treated conditions highlights the effectiveness of this multiplex approach in identifying optimal ligand combinations for differentiating between conditions.

These findings highlight the potential of NBA platform for multiplexed EV analysis. The combined approach provides a deeper understanding of the changes in EV subpopulations, either related to the appearance of a new population or the modification of the existing population, and their biophysical properties, offering a foundation for identifying biomarkers associated with cellular responses to cytotoxic stress.

5. Conclusions

This study explored the capabilities of the NBA platform to phenotype EVs derived from HMEC-1 cells, focusing on the impact of B[a]P-induced cytotoxicity on surface protein expression. A miniaturized biochip design was developed, enabling simultaneous analysis of 11 ligands, including a negative control, on the same platform. SPRi experiments revealed significant differences in responses for Anti-CD36, Anti-CD81, and Anti-ApoA, suggesting their association with B[a]P exposure. Complementary AFM analysis and statistical evaluation highlighted size-related differences between treated and control EVs, identifying Anti-CD81, Anti-ApoA, Annexin-V, Anti-NOX2, and Anti-VEGFR1 as potential biomarkers for the cytotoxic condition. These findings suggest that B[a]P exposure not only increases EV size but also selectively alters the expression of key surface markers, reflecting shifts in the phenotypic profile of 10K EVs. The combined use of SPRi and AFM emphasizes the potential of lEV-specific markers to uncover phenotypic changes associated with cytotoxic stress, offering valuable insights into EV heterogeneity and their role in cellular stress responses.

This method is both comprehensive and highly versatile, making it easily adaptable to other nano-bioparticles models. With further expansion of the ligand panel, this platform has the potential to go beyond addressing biological questions, evolving into a powerful diagnostic tool for identifying disease-specific EV phenotypes and biomarkers.

Author Contributions: For research articles with several authors, a short paragraph specifying their individual contributions must be provided. The following statements should be used "Conceptualization, G.R., C.E-C., W.B.; methodology, G.R., C.E-C., W.B.; investigation, G.R.; resources, A.R., J.G., E.LF.; writing—original draft preparation, G.R..; writing—review and editing, C.E-C, E.LF., J.G., and W.B..; supervision, E.L., W.B., and C.E-C..; funding acquisition, C.E-C.. All authors have read and agreed to the published version of the manuscript."

Funding: This research was funded by the NOVICE project supported by the EIPHI Graduate School (contract ANR-17-EURE-0002) and by the ENDOMITOPAH project supported by the French National Agency for Research (ANR; R23137NN).

Institutional Review Board Statement: Not applicable.

Data Availability Statement: The original contributions presented in the study are included in the article, further inquiries can be directed to the corresponding author.

Acknowledgments: The authors wish to thank the laboratory staff of the Clinical-Innovation Proteomic Platform (CLIPP) and Nano2BIO team at FEMTO-ST Institute for fruitful discussion and technical/instrumental supports.

 doi:10.20944/preprints202501.0599.v1

Conflicts of Interest: The authors declare no conflicts of interest.

References

1. M. Simons and G. Raposo, 'Exosomes--vesicular carriers for intercellular communication', *Curr Opin Cell Biol*, vol. 21, no. 4, pp. 575–581, Aug. 2009, doi: 10.1016/j.ceb.2009.03.007.
2. D. Petroni, C. Fabbri, S. Babboni, L. Menichetti, G. Basta, and S. Del Turco, 'Extracellular Vesicles and Intercellular Communication: Challenges for In Vivo Molecular Imaging and Tracking', *Pharmaceutics*, vol. 15, no. 6, p. 1639, Jun. 2023, doi: 10.3390/pharmaceutics15061639.
3. M. P. Zaborowski, L. Balaj, X. O. Breakefield, and C. P. Lai, 'Extracellular Vesicles: Composition, Biological Relevance, and Methods of Study', *Bioscience*, vol. 65, no. 8, pp. 783–797, Aug. 2015, doi: 10.1093/biosci/biv084.
4. W. Liang *et al.*, 'Mitochondria are secreted in extracellular vesicles when lysosomal function is impaired', *Nat Commun*, vol. 14, no. 1, p. 5031, Aug. 2023, doi: 10.1038/s41467-023-40680-5.
5. C. M. Eckhardt, A. A. Baccarelli, and H. Wu, 'Environmental Exposures and Extracellular Vesicles: Indicators of Systemic Effects and Human Disease', *Curr Environ Health Rep*, vol. 9, no. 3, pp. 465–476, Sep. 2022, doi: 10.1007/s40572-022-00357-5.
6. T. Ohura, T. Amagai, M. Fusaya, and H. Matsushita, 'Polycyclic aromatic hydrocarbons in indoor and outdoor environments and factors affecting their concentrations', *Environ Sci Technol*, vol. 38, no. 1, pp. 77–83, Jan. 2004, doi: 10.1021/es030512o.
7. F. Henkler, K. Stolpmann, and A. Luch, 'Exposure to polycyclic aromatic hydrocarbons: bulky DNA adducts and cellular responses', *Exp Suppl*, vol. 101, pp. 107–131, 2012, doi: 10.1007/978-3-7643-8340-4_5.
8. B. J. Benedikter, A. R. Weseler, E. F. M. Wouters, P. H. M. Savelkoul, G. G. U. Rohde, and F. R. M. Stassen, 'Redox-dependent thiol modifications: implications for the release of extracellular vesicles', *Cell Mol Life Sci*, vol. 75, no. 13, pp. 2321–2337, Jul. 2018, doi: 10.1007/s00018-018-2806-z.
9. F. Bewicke-Copley *et al.*, 'Extracellular vesicles released following heat stress induce bystander effect in unstressed populations', *J of Extracellular Vesicle*, vol. 6, no. 1, p. 1340746, Dec. 2017, doi: 10.1080/20013078.2017.1340746.
10. K. P. De Sousa, I. Rossi, M. Abdullahi, M. I. Ramirez, D. Stratton, and J. M. Inal, 'Isolation and characterization of extracellular vesicles and future directions in diagnosis and therapy', *Wiley Interdiscip Rev Nanomed Nanobiotechnol*, vol. 15, no. 1, p. e1835, Jan. 2023, doi: 10.1002/wnan.1835.
11. J. Suthar, M. Taub, R. P. Carney, G. R. Williams, and S. Guldin, 'Recent developments in biosensing methods for extracellular vesicle protein characterization', *Wiley Interdiscip Rev Nanomed Nanobiotechnol*, vol. 15, no. 1, p. e1839, Jan. 2023, doi: 10.1002/wnan.1839.
12. L. K. Chin *et al.*, 'Plasmonic Sensors for Extracellular Vesicle Analysis: From Scientific Development to Translational Research', *ACS Nano*, vol. 14, no. 11, pp. 14528–14548, Nov. 2020, doi: 10.1021/acsnano.0c07581.
13. D. L. M. Rupert *et al.*, 'Determination of Exosome Concentration in Solution Using Surface Plasmon Resonance Spectroscopy', *Anal. Chem.*, vol. 86, no. 12, pp. 5929–5936, Jun. 2014, doi: 10.1021/ac500931f.
14. B. Szymanska, Z. Lukaszewski, B. Zelazowska-Rutkowska, K. Hermanowicz-Szamatowicz, and E. Gorodkiewicz, 'An SPRi Biosensor for Determination of the Ovarian Cancer Marker HE4 in Human Plasma', *Sensors*, vol. 21, no. 10, p. 3567, May 2021, doi: 10.3390/s21103567.
15. B. Szymańska, Z. Lukaszewski, K. Hermanowicz-Szamatowicz, and E. Gorodkiewicz, 'A biosensor for determination of the circulating biomarker CA125/MUC16 by Surface Plasmon Resonance Imaging', *Talanta*, vol. 206, p. 120187, Jan. 2020, doi: 10.1016/j.talanta.2019.120187.
16. S. Picciolini *et al.*, 'An SPRi-based biosensor pilot study: Analysis of multiple circulating extracellular vesicles and hippocampal volume in Alzheimer's disease', *J Pharm Biomed Anal*, vol. 192, p. 113649, Jan. 2021, doi: 10.1016/j.jpba.2020.113649.
17. C.-C. Hsu *et al.*, 'Simultaneous Detection of Tumor Derived Exosomal Protein-MicroRNA Pairs with an Exo-PROS Biosensor for Cancer Diagnosis', *ACS Nano*, vol. 17, no. 9, pp. 8108–8122, May 2023, doi: 10.1021/acsnano.2c10970.

18. S. Obeid *et al.*, 'NanoBioAnalytical characterization of extracellular vesicles in 75-nm nanofiltered human plasma for transfusion: A tool to improve transfusion safety', *Nanomedicine: Nanotechnology, Biology and Medicine*, vol. 20, p. 101977, Aug. 2019, doi: 10.1016/j.nano.2019.02.026.
19. G. Raizada *et al.*, 'Multimodal Analytical Platform on a Multiplexed Surface Plasmon Resonance Imaging Chip for the Analysis of Extracellular Vesicle Subsets', *JoVE*, no. 193, p. 64210, Mar. 2023, doi: 10.3791/64210.
20. M. Le Goff *et al.*, 'PAHs increase the production of extracellular vesicles both in vitro in endothelial cells and in vivo in urines from rats', *Environmental Pollution*, vol. 255, p. 113171, Dec. 2019, doi: 10.1016/j.envpol.2019.113171.
21. J. A. Welsh *et al.*, 'Minimal information for studies of extracellular vesicles (MISEV2023): From basic to advanced approaches', *J Extracell Vesicles*, vol. 13, no. 2, p. e12404, Feb. 2024, doi: 10.1002/jev2.12404.
22. F. Remy-Martin *et al.*, 'Surface plasmon resonance imaging in arrays coupled with mass spectrometry (SUPRA–MS): proof of concept of on-chip characterization of a potential breast cancer marker in human plasma', *Anal Bioanal Chem*, vol. 404, no. 2, pp. 423–432, Aug. 2012, doi: 10.1007/s00216-012-6130-4.
23. G. Raizada *et al.*, 'Raman spectroscopy of large extracellular vesicles derived from human microvascular endothelial cells to detect benzo[a]pyrene exposure', *Anal Bioanal Chem*, vol. 416, no. 28, pp. 6639–6649, Nov. 2024, doi: 10.1007/s00216-024-05567-4.
24. D. P. Ramakrishnan, R. A. Hajj-Ali, Y. Chen, and R. L. Silverstein, 'Extracellular Vesicles Activate a CD36-Dependent Signaling Pathway to Inhibit Microvascular Endothelial Cell Migration and Tube Formation', *ATVB*, vol. 36, no. 3, pp. 534–544, Mar. 2016, doi: 10.1161/ATVBAHA.115.307085.
25. H. Farhangkhoee, Z. A. Khan, Y. Barbin, and S. Chakrabarti, 'Glucose-induced up-regulation of CD36 mediates oxidative stress and microvascular endothelial cell dysfunction', *Diabetologia*, vol. 48, no. 7, pp. 1401–1410, Jul. 2005, doi: 10.1007/s00125-005-1801-8.
26. S. Zhou *et al.*, 'Association between polycyclic aromatic hydrocarbon exposure and blood lipid levels: the indirect effects of inflammation and oxidative stress', *Environ Sci Pollut Res*, vol. 30, no. 59, pp. 123148–123163, Nov. 2023, doi: 10.1007/s11356-023-31020-7.
27. I. Suc, I. Escargueil-Blanc, M. Troly, R. Salvayre, and A. Nègre-Salvayre, 'HDL and ApoA Prevent Cell Death of Endothelial Cells Induced by Oxidized LDL', *ATVB*, vol. 17, no. 10, pp. 2158–2166, Oct. 1997, doi: 10.1161/01.ATV.17.10.2158.
28. L. Rakateli, R. Huchzermeier, and E. P. C. Van Der Vorst, 'AhR, PXR and CAR: From Xenobiotic Receptors to Metabolic Sensors', *Cells*, vol. 12, no. 23, p. 2752, Nov. 2023, doi: 10.3390/cells12232752.
29. N. Van Meteren *et al.*, 'Extracellular vesicles released by polycyclic aromatic hydrocarbons-treated hepatocytes trigger oxidative stress in recipient hepatocytes by delivering iron', *Free Radical Biology and Medicine*, vol. 160, pp. 246–262, Nov. 2020, doi: 10.1016/j.freeradbiomed.2020.08.001.